






Exploring the A-V-Sb landscape beyond  $AV_3Sb_5$ : A case study on the  $KV_6Sb_6$  Kagome compoundAishwarya Mantravadi <sup>1</sup>, Volodymyr Gvozdetyskiy,<sup>1,\*</sup> Arka Sarkar <sup>1,2</sup>, Yaroslav Mudryk <sup>2</sup>, and Julia V. Zaikina <sup>1,†</sup><sup>1</sup>Department of Chemistry, Iowa State University, Ames, Iowa 50011, USA<sup>2</sup>Ames National Laboratory of US DOE, Iowa State University, Ames, Iowa 50011, USA (Received 26 May 2023; revised 30 August 2023; accepted 6 October 2023; published 15 November 2023)

Kagome compounds have garnered attention in the past few years for their intriguing magnetic properties arising from spin frustration dictated by the geometry of the Kagome sublattice. In this paper, we highlight the success of the unconventional hydride route for the fast and easy synthesis of the Kagome compound  $KV_6Sb_6$ . High-temperature *in situ* powder x-ray diffraction (PXRD) studies proved to be useful in hinting at the existence of  $KV_6Sb_6$ , identifying its synthesis conditions, and understanding the reaction mechanism. The crystal structure for  $KV_6Sb_6$  was determined from high-resolution PXRD data. The compound has a layered structure [ $R\bar{3}m$ ,  $a = 5.5318(9)$  Å,  $c = 34.23(3)$  Å,  $V = 907.0(8)$  Å<sup>3</sup>,  $Z = 3$  at room temperature] and features a Kagome bilayer of V atoms.  $KV_6Sb_6$  is isostructural to the previously reported  $RbV_6Sb_6$  and  $CsV_6Sb_6$  compounds.  $KV_6Sb_6$  is thermally stable in vacuum up to 1173 K, as evident from the high-temperature *in situ* PXRD and differential scanning calorimetric analysis. Investigation of magnetic properties for  $KV_6Sb_6$  between 2 and 300 K reveals temperature-independent paramagnetism and an absence of superconductivity, like the Rb and Cs analogs. Furthermore, we compare the magnetic properties of  $KV_3Sb_5$ , another ternary Kagome compound, synthesized via two different methods: the hydride route and the traditional route from elements. Low-temperature transport property measurements of  $KV_6Sb_6$  indicate metallic behavior and an intrinsically low thermal conductivity of  $1.0 \text{ W K}^{-1} \text{ m}^{-1}$  at 300 K. The layered structure of  $KV_6Sb_6$  makes it an attractive candidate for deintercalation and doping studies to tune both magnetic and transport properties, laying a foundation for further studies.

DOI: [10.1103/PhysRevMaterials.7.115002](https://doi.org/10.1103/PhysRevMaterials.7.115002)

## I. INTRODUCTION

Investigation of the structure-property relationships in inorganic solids is crucial for pinpointing the unique structural features that can yield interesting magnetic properties. Several materials classes have been extensively studied in the pursuit of discovering and realizing intriguing magnetic behavior; one such example is the Kagome class of compounds. A Kagome lattice has a starlike geometric pattern comprising regular hexagons and triangles [1,2]. Structures of most of the Kagome compounds belong to the  $R\bar{3}m$ ,  $P6/mmm$ , or  $P6_3/mmc$  space groups, a consequence of the geometry of the Kagome sublattice [2,3]. This geometry inhibits perfect antiferromagnetic alignment of spins at the Kagome sites, causing magnetic frustration. Magnetic frustration contributes to the origin of distinctive electronic and magnetic characteristics found in the Kagome materials, such as superconductivity, quantum spin liquids, charge density wave (CDW) order, and Dirac fermions [3–8]. Research efforts, both experimental and computational, have been geared toward an in-depth study of the influence of the structural features and bonding on the band structure for accurate and accelerated prediction of Kagome candidates [2,3].

The exotic magnetic characteristics rendered possible by the geometry of the Kagome lattice have triggered a quest for prototype Kagome materials capable of realizing interesting physical properties. This quest has led to realizing Kagome nets in jarosite [1,2,9–14], pyrochlores [1,2,15–23], herberthsmithites [3,24,25], intermetallic Kagome compounds such as  $HoAgGe$  [26],  $PrPdAl$  [27],  $DyNi_5Ge_3$  [28], and most recently, the family of intermetallic compounds  $AV_3Sb_5$  ( $A = K, Rb, Cs$ ) [29]. The  $AV_3Sb_5$  compounds crystallize in the  $P6/mmm$  space group and have a layered structure consisting of a Kagome lattice of vanadium atoms. Extensive work has been conducted to understand the electronic and magnetic properties of these compounds [30–43]. Shortly after their discovery, superconductivity was unearthed in these compounds:  $KV_3Sb_5$ ,  $T_C = 0.92$  K;  $RbV_3Sb_5$ ,  $T_C = 0.93$  K; and  $CsV_3Sb_5$ ,  $T_C = 2.5$  K [30–33]. Studies have also revealed unconventional chiral CDW order in this family of alkali metal-vanadium antimonides:  $KV_3Sb_5$ ,  $T_{CDW} = 78$  K;  $RbV_3Sb_5$ ,  $T_{CDW} = 103$  K; and  $CsV_3Sb_5$ ,  $T_{CDW} = 94$  K [34–38]. Furthermore, the energy of the Fermi level ( $E_F$ ) was adjusted via doping to tune the superconducting transition temperature [39–43]. Recently, the isostructural  $ATi_3Bi_5$  ( $A = Rb, Cs$ ) compounds were reported, extending the family to the bismuthides [44–49].

The attractive science of the magnetic and electronic states in  $AV_3Sb_5$  compounds fueled the search for new compounds in the A-V-Sb systems. This resulted in the discovery of two families of compounds, namely,  $AV_8Sb_{12}$  ( $A = Rb, Cs$ )

\*Present Address: Department of Chemistry, University of Alberta, Edmonton, Alberta, Canada T6G 2G2.

†[yaikina@iastate.edu](mailto:yaikina@iastate.edu)

and  $AV_6Sb_6$  ( $A = K, Rb, Cs$ ) [50–53]. The  $AV_8Sb_{12}$  and  $AV_6Sb_6$  compounds also have a layered structure with a single Kagome layer of vanadium atoms in  $AV_8Sb_{12}$  and a Kagome bilayer of vanadium atoms in  $AV_6Sb_6$ . Although the  $AV_8Sb_{12}$  and  $AV_6Sb_6$  compounds are not superconducting under ambient conditions, superconductivity can be realized in  $AV_6Sb_6$  under pressure ( $A = K, Rb, Cs$ ) [52]. Detailed reports describing the flux crystal growth, crystal structures, and properties can be found for the Rb and Cs analogs for the  $AV_6Sb_6$  compounds; however, experimental details for the K analog ( $KV_6Sb_6$ ) are lacking [50–53].

While the quest for Kagome materials or any new material is exciting, material synthesis is often challenging owing to the poor kinetics and high diffusion barriers of solid-state reactions [54–56]. This holds particularly true for the  $A$ - $T$ - $Sb$  ternary systems with early transition metals ( $A = Li, Na, K, Cs, Rb$ ;  $T = Ti, V, Cr$ ) due to the extreme difference in the reactivity of  $A$  (melting point (m.p.): 300–453 K),  $T$  (m.p. 1941–2183 K), and  $Sb$  (m.p. 903 K). In the  $A$ - $T$ - $Sb$  ternary systems only 10 compounds are known, mostly with vanadium [29,44–53]. The traditional solid-state synthesis, also referred to as the *heat-and-beat* method, requires high temperatures and long annealing times to facilitate diffusion. Unconventional precursors can aid in overcoming the limitations posed by traditional routes. One such synthetic method is the hydride route, in which the soft alkali metal is replaced with its saltlike reactive alkali metal hydride [57–63]. The use of hydride allows for precise compositional control while intimate mixing of precursors via ball milling facilitates diffusion. Switching the alkali metal for its hydride typically leads to faster reactions at lower temperatures than traditional solid-state synthetic routes. The hydride route also allows for synthesizing ternary phases composed of elements with significantly different reactivities [59,60] and enables access to metastable phases [60]. Therefore, the hydride route is ideal for rapid phase exploration.

Herein, we report on the hydride route as a fast and easy alternative for the synthesis of the  $KV_6Sb_6$  compound in the form of microcrystalline powder. We present a detailed study of  $KV_6Sb_6$  synthesis, crystal structure, and low-temperature magnetic and transport properties. Our advanced synthesis approach, guided by *in situ* studies and compositional prediction via machine learning algorithm [64,65], proved to be a powerful tool for probing the  $K$ - $V$ - $Sb$  system in search of compounds.

## II. EXPERIMENT

### A. Chemicals

Vanadium powder (V, Alfa Aesar, 99.5%) was used as received. Potassium hydride powder (KH, 30 wt. % dispersion in mineral oil, Sigma-Aldrich) was washed several times with toluene and dried in vacuum before use. Antimony powder was obtained by ball milling Sb shots (Sb, Alfa Aesar, 99.9999%) using a SPEX mixer/mill 8000M for 60 min in a ball mill container with tungsten carbide (WC) inserts and two WC balls. All starting materials and samples were handled in an argon-filled glovebox with  $p(O_2) < 1$  ppm and  $p(H_2O) < 1$  ppm.

### B. Synthesis

Synthesis of polycrystalline samples was carried out using the hydride route. For synthesis of  $KV_3Sb_5$  and  $KV_6Sb_6$ , powders of KH, V, and Sb were weighed in the desired molar ratio (total mass = 0.3 g) and loaded into a polycarbonate grinding vial with a methacrylate grinding ball. For  $V_3Sb_2$ , V and Sb powders were used for synthesis. The grinding vial was sealed into two polyethylene bags under argon atmosphere, and the mixture was ball milled using a SPEX mixer/mill 8000M for 6 min. The ball-milled powders were transferred to a tantalum tube (ID: 8.2 mm, OD: 9.4 mm; length:  $\sim 45$  mm), which was sealed using an arc welder under argon atmosphere and then put into a silica reactor. The reactor is equipped with a Swagelok safety check valve to avoid overpressurizing from the hydrogen gas released during the reaction. The setup was evacuated down to  $2.7 \times 10^{-5}$  to  $3.0 \times 10^{-5}$  Bar pressure and placed into a programmable high-temperature furnace. For  $KV_6Sb_6$  and  $V_3Sb_2$ , the furnace was heated from room temperature (RT) to 1073 K in 5 h, was held at this temperature for 72 h, and was then allowed to cool naturally back to RT. For  $KV_3Sb_5$ , a furnace was heated from RT to 873 K in 5 h and was held at this temperature for 24 h before being cooled to RT. A side reaction of Sb with the Ta tube resulted in the formation of the Ta-Sb binaries as impurities in the thus-obtained samples. Therefore, a BN crucible with a lid (OD: 7 mm, ID: 5 mm, length: 25 mm/30 mm) sealed into a niobium tube was used as an alternative to the sealed Ta tube. The rest of the synthesis steps remained the same. It should be noted that both Nb and Ta tubes are permeable to hydrogen [66–68], which can eventually escape through the check valve.

### C. Powder x-ray diffraction (PXRD)

The purity of synthesized samples and identity of crystalline phases were confirmed by powder x-ray diffraction (PXRD) using a Rigaku MiniFlex600 powder diffractometer with Cu  $K\alpha$  radiation ( $\lambda = 1.54051 \text{ \AA}$ ) and Ni  $K\beta$  filter. Data were collected on a zero-background plate holder in air. For air-sensitive samples, powders were loaded onto nonzero background air-sensitive holders in Ar filled glovebox to avoid oxidation during the PXRD data collection. Phase analysis was performed using the COD database incorporated into the Match-3! software [69].

### D. In situ high-temperature PXRD (HT-PXRD)

High-temperature synchrotron x-ray diffraction data were collected at the synchrotron beamline 17-BM at the Advanced Photon Source at Argonne National Lab (APS ANL) at  $\lambda = 0.24087 \text{ \AA}$ . A thick-wall (0.1 mm) silica capillary (0.7 mm outer diameter) was filled with a finely ground sample of  $KV_6Sb_6$  to a height of 10 mm and was flame-sealed under vacuum. The capillary was mounted into a secondary shield capillary located on a sample stage equipped with two resistive microheaters and a thermocouple set as close as possible to the measurement area. Data were collected every 1 min upon heating and cooling in the temperature range of 298–1245–298 K with heating and cooling at a rate of  $10 \text{ K min}^{-1}$ .

Further details of this experimental setup can be found elsewhere [70].

To study the hydride reaction, the desired molar ratio of KH, V, and Sb powders were weighed and ball milled for 6 min in the SPEX mixer/mill 8000M. A silica capillary (dimensions as specified above) was filled with the ball-milled precursors to a height of 10 mm and was sealed under a vacuum at the height of 50 mm to provide enough headspace. This was done to avoid rupture of the capillary due to over pressurization caused by the release of hydrogen gas during the reaction. The capillary was placed vertically in the x-ray beam during the analysis, and PXRD data were collected every 1 min as the sample was heated and cooled at a rate of 20 K/min in the temperature range of 298–1173–298 K.

### E. RT high-resolution PXRD (HR-PXRD)

High-resolution synchrotron powder diffraction data were collected at beamline 11-BM APS ANL at 298 K and  $\lambda = 0.45198 \text{ \AA}$  for a powdered sample of  $\text{KV}_6\text{Sb}_6$ . The sample was loaded into a 0.7 mm outer diameter, thick-wall (0.1 mm) silica capillary that was flame-sealed under vacuum. The capillary was placed inside a Kapton tube, fixed on the mounting base, and covered with a magnetic cap of the sample holder provided by APS ANL.

### F. Structure determination

The program FOX [71] for the *ab initio* structure determination from high-resolution PXRD (HR-PXRD) data was used for indexing and initial structure determination. The powder pattern was indexed as a monoclinic unit cell ( $a = 9.578082 \text{ \AA}$ ,  $b = 5.532909 \text{ \AA}$ ,  $c = 11.868462 \text{ \AA}$ , and  $\beta = 105.95^\circ$ ), space group  $C2/m$  (#12), yet the lower-symmetry space group  $C2$  (#5), which is a subgroup of  $C2/m$ , was considered for the structure solution. Positions of heavier Sb and V atoms were obtained first: three Sb sites ( $4c$ ,  $4c$ , and  $4c$ ) and three V sites ( $4c$ ,  $4c$ , and  $4c$ ). In subsequent refinement steps, lighter K atoms were placed in the centers of hexagonal prisms formed by Sb atoms upon consideration of typical coordination environment ( $2a$  site). Analysis of this model indicated that, indeed, the higher-symmetry space group  $C2/m$  (initially suggested by FOX) can be considered with K atoms occupying a  $2a$  site, Sb atoms occupying three  $4i$  sites, and V atoms in  $4i$  and  $8j$  sites. This model was further refined by the Rietveld method using the JANA 2006 software package [72], providing a satisfactory fit. Parameters such as preferred orientation, peak shape, background coefficients, lattice parameters, atomic coordinates, atomic displacement parameters (ADPs), and occupancy were refined. This refined model ( $C2/m$ ) was analyzed by Platon [73] for higher symmetry. As a result, a structural model in the  $R$ -rhombohedral unit cell ( $a = 5.53333 \text{ \AA}$ ,  $c = 34.2233 \text{ \AA}$ ) in the  $R\bar{3}m$  (#166) space group was suggested.  $\text{KV}_6\text{Sb}_6$  is isostructural to  $\text{CsV}_6\text{Sb}_6$  and  $\text{RbV}_6\text{Sb}_6$  compounds [50–53] and the structure of  $\text{KV}_6\text{Sb}_6$  was determined independently in this paper. The  $R\bar{3}m$  model has K atoms in a  $3a$  site, V atoms in a  $18h$  site, while Sb atoms occupy three  $6c$  sites. Details of data collection and refinement are provided in Table S1 in the Supplemental Material [74]. Table S2 in the Supplemental Material [74] lists the atomic

coordinates, site multiplicity, and ADPs of all the atomic sites in the structure.

### G. Spark plasma sintering (SPS)

Consolidation of  $\text{KV}_6\text{Sb}_6$  powder was performed via spark plasma sintering (SPS) using Dr. Sinter Lab Jr. SPS-211Lx (Sumitomo Coal Mining Co., Ltd.). The powdered sample was loaded into a small graphite die (inner diameter = 5 mm; length = 15 mm) in an argon atmosphere. Two circular graphite foils of 5 mm diameter were placed above and below the powder in the die. Tungsten carbide plungers were inserted on either side of the die to press and hold the powder in place. The assembled smaller die was further inserted into a larger outer graphite die with graphite plungers (inner diameter = 20 mm; length = 40 mm). The samples were sintered by heating to 773 K over a period of 9 min under a uniaxial pressure of 117 MPa, followed by dwelling at 773 K for 5 min. Thereafter, the pressure was released, and the sample was allowed to cool to RT. In the glovebox, the pellets were removed from the graphite die and polished to remove traces of the graphite foil stuck to the pellet surface. The geometrical density of the pellets was measured to be 93–95% of the crystallographic density.

### H. Magnetic property measurement

Magnetic measurement was performed on powders of  $\text{KV}_6\text{Sb}_6$ ,  $\text{V}_3\text{Sb}_2$ , and  $\text{KV}_3\text{Sb}_5$ . To avoid oxidation of  $\text{KV}_6\text{Sb}_6$ , a  $\sim 50$  mg polycrystalline sample was transferred to an EPR tube in an argon-filled glovebox, which was further sealed under a vacuum.  $\text{V}_3\text{Sb}_2$  and  $\text{KV}_3\text{Sb}_5$  powders were packed into gel capsules. Measurements were carried out using Quantum Design MPMS XL-7 and MPMS3 SQUID magnetometers. The dc magnetic susceptibility measurements were carried out at 0.01, 0.1, and 2 T constant applied magnetic field in a temperature range of 2–300 K, while the ac susceptibility measurements were carried out at a frequency of 100 Hz between 2–50 K (for  $\text{KV}_6\text{Sb}_6$ ) and 2–100 K (for  $\text{KV}_3\text{Sb}_5$ ) using  $H_{ac} = 5 \text{ Oe}$ .

### I. Thermoelectric properties measurement

Low-temperature transport properties of a  $\text{KV}_6\text{Sb}_6$  pellet sintered by SPS were measured in a temperature range of 2–300 K using the commercial multipurpose Physical Properties Measurement System Evercool I (PPMS, Quantum Design). The Seebeck coefficient ( $S$ ) and thermal conductivity ( $\kappa$ ) were measured using the thermal transport option in a two-probe configuration. Electrical resistivity ( $\rho$ ) was measured using the electrical transport option in a four-probe geometric setup, using 50  $\mu\text{m}$  platinum wires attached with silver paste.

### J. Formation energy calculation and heat map construction

An online formation energy predictor tool [64] was utilized for the calculation of the formation energies of various compositions in the K-V-Sb system. This predictor uses a machine learning approach [64,65], where a large set of data (composition and formation energy), containing output from  $\sim 15000$  density functional theory (DFT) calculations for a

wide range of chemical systems, is used as input for the predictive model [65]. Formation energies are then predicted for arbitrary compositions independent of structural input using machine learning only, without performing DFT calculations for the selected chemistries. In this paper, formation energies were calculated for  $\sim 1000$   $K_xV_ySb_z$  compositions at a 1–2 at. % increment. These values were then used to construct a heat map that is a ternary contour plot of formation energy as a function of composition.

### K. Energy dispersive x-ray (EDX) scanning electron microscopy

Elemental analysis was performed using a JEOL JSM-IT200 scanning electron microscope (SEM) equipped with a JEOL energy-dispersive x-ray (EDX) analysis system with a silicon drift detector. Powder samples and pellets were adhered to aluminum stubs using carbon tape and then placed into an aluminum holder for insertion into the SEM. Samples were oriented perpendicular to the beam and analyzed using a 10–20 kV accelerating voltage with an accumulation time of 60 s.

### L. Differential scanning calorimetry (DSC)

Differential scanning calorimetry (DSC) measurement was performed using a Netzsch 404 F3 Pegasus Differential Scanning Calorimeter. A powdered sample ( $m = 40$  mg) was sealed inside an evacuated silica ampoule, heated to 1173 K, and cooled to 373 K at a rate of  $10 \text{ K min}^{-1}$ .

## III. RESULTS AND DISCUSSION

### A. Synthesis

Interest in ternary alkali metal antimonides containing early  $3d$  metals was sparked with the discovery of the  $AV_3Sb_5$  compounds [29–33]. Flux growth using the low-melting eutectic between  $KSb_2$ –Sb or  $KSb_2$ –KSb and traditional synthesis from elements was employed to synthesize the  $AV_3Sb_5$  compounds [29]. We were interested in further probing the A–V–Sb systems using the hydride route, where ductile alkali metal  $A$  is replaced with its saltlike hydride  $AH$ . Use of the hydride route allowed for rapid phase screening of various compositions in the K–V–Sb system. The exact composition could be precisely targeted owing to the mixable, saltlike KH precursor as opposed to ductile and soft K metal. Synthesis was guided by *in situ* studies for finetuning the reaction parameters to yield a phase-pure sample of the  $KV_6Sb_6$  compound, enabling the measurement of magnetic and transport properties.

Initially, the hydride route was utilized to synthesize the previously reported  $KV_3Sb_5$  ternary compound [29]. When precursors mixed in a nominal loading molar ratio of  $KH : V : Sb = 1 : 3 : 5$  were heated at 873 K for 24 h in a sealed Ta tube, a sample of  $KV_3Sb_5$  was obtained. This validated the use of the hydride route to produce crystalline ternary compounds comprising elements with drastically different reactivities (m.p. K = 337 K, m.p. V = 2183 K, and m.p. Sb = 903 K). The use of KH instead of K allowed for shorter

milling time (6 vs 60 min) and annealing duration (24 vs 48 h) compared with the previously reported method [29].

To evaluate the thermal stability of  $KV_3Sb_5$ , we collected *in situ* high-temperature PXRD data for  $KV_3Sb_5$  [Fig. 1(a)]. The  $KV_3Sb_5$  compound is thermally stable up to 1000 K in a capillary sealed under vacuum. Upon heating  $> 1000$  K, a new set of diffraction peaks was observed  $\sim 1073$  K [Fig. 1(a), purple region]. This hinted at the existence of a new ternary phase in the system. Figure 1(b) highlights the 954–1154 K region where the transformation of the  $KV_3Sb_5$  phase to the new ternary phase is observed. Based on this observation, the synthesis temperature for the new phase was kept within the 973–1173 K range.

With the hints of a new phase and a good estimate of the temperatures to be used for its synthesis, we used a computational heat map of the K–V–Sb system as a guide to narrow down the compositional phase space for further exploration (Fig. 2) [64,65]. In a heat map, the compositions that fall into regions of low-formation energy are suggestive of a stable compound. For the K–V–Sb system, known phases in this or similar systems (i.e., the  $KV_3Sb_5$  [29] and  $(Rb/Cs)V_8Sb_{12}$  [50] phases) lie in the negative (low) formation energy region. Based on these predictions, several compositions (represented as blue circles in Fig. 2) were attempted in addition to the  $KV_3Sb_5$  stoichiometry. Characteristic diffraction peaks for the new ternary phase were first observed in the sample with a loading molar ratio of  $KH : V : Sb = 1 : 2 : 2$  heated at 973 K for 72 h. The diffraction peaks were broad, signaling low crystallinity of the phase, and were accompanied by the peaks of  $V_3Sb$  impurity. This implied a need to tune both the synthesis composition and temperature to obtain a single-phase crystalline sample of the new phase. The SEM-EDX study of the sample with a considerable molar fraction of the new ternary phase revealed the  $V : Sb$  ratio to be 1:1. Therefore, when the K content was lowered, maintaining the  $V : Sb$  molar ratio at 1:1 (molar ratio of  $KH : V : Sb = 1.4 : 6 : 6$ ), and the synthesis temperature was increased to 1073 K, consistent with high-temperature PXRD data, a crystalline single-phase sample of the target new ternary phase was obtained. Crystal structure solved using high-resolution synchrotron PXRD data determined the new ternary phase to have the composition  $KV_6Sb_6$  (Fig. 3, PXRD pattern in black), which is close to the loading molar ratio of  $KH : V : Sb = 1.4 : 6 : 6$ .

Note that excess KH with respect to the stoichiometric 1:6:6 composition is required for synthesis and is crucial for preparation of a single-phase sample. As indicated in Fig. 3 (PXRD pattern in blue), a nominal composition of  $KH : V : Sb = 1 : 6 : 6$  yields the  $KV_6Sb_6$  compound but with broader, unresolved diffraction peaks at  $Q \sim 1.8, 3,$  and  $3.7 \text{ \AA}^{-1}$ , highlighted in yellow (Fig. 3). The diffraction peaks remain broad even after the second annealing, as seen in Fig. S1(a) in the Supplemental Material [74]. In fact, the formation of  $KV_6Sb_6$  is extremely sensitive to the amount of K loaded for the reaction. Figure S1(a) in the Supplemental Material [74] shows the PXRD data for reactions with variation in KH content, i.e.,  $K_{1+x}V_6Sb_6$  ( $x = 0, 0.2, 0.4,$  and  $0.6$ ). With an increase in K content, the diffraction peaks at  $Q \sim 1.8, 3,$  and  $3.7 \text{ \AA}^{-1}$  (highlighted in yellow in Fig. S1(a) in the Supplemental Material [74] and Fig. 3) appear well resolved. With a decrease in the K content, an additional peak appears between

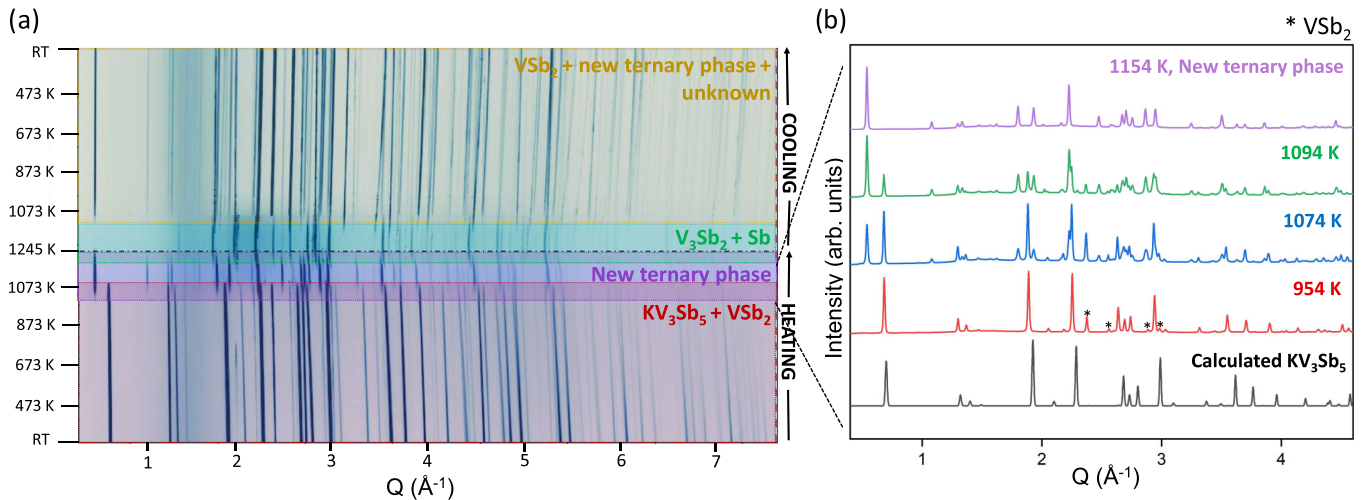


FIG. 1. (a) High-temperature *in situ* synchrotron powder x-ray diffraction (PXRD) data for  $KV_3Sb_5$  in the form of a waterfall plot displays sequential changes in the PXRD patterns, collected upon heating and cooling. Each vertical line represents a diffraction peak in the PXRD pattern. Distinct temperature ranges with the indicated phases present are highlighted in red, purple, green, and yellow. (b) Selected PXRD patterns in the 954–1154 K range indicating the transformation of  $KV_3Sb_5$  into  $KV_6Sb_6$ .

the highlighted set of two peaks (making them appear broader and unresolved), suggesting formation of a structurally related phase with reduced K content, i.e.,  $K_{1-y}V_6Sb_6$  [74]. The difference in the intensity between observed and calculated diffraction peaks at  $Q \sim 0.6 \text{ \AA}^{-1}$  (highlighted in blue, Fig. 3) is attributed to preferred orientation in the sample. Refer to Fig. S2 in the Supplemental Material [74] for further details.

To prove that  $KV_6Sb_6$  is not an H-stabilized phase, reactions were carried out with K metal under identical reaction

conditions. Indeed, the  $KV_6Sb_6$  phase forms albeit along with a  $KV_3Sb_5$  impurity (Fig. S1(b) in the Supplemental Material [74]). We hypothesize that the use of elemental K instead of the hydride does not allow for sufficient initial mixing of the precursors. Thus, the synthesis proceeds with diffusion limitation through the formation of a more K- and Sb-rich  $KV_3Sb_5$  ternary phase first, resulting in a multiphase sample under identical reaction conditions. There is no variation in unit cell parameters (within estimated standard deviation (e.s.d.)) for  $KV_6Sb_6$  prepared using elemental K or KH, suggesting that H is not incorporated in the interstitial sites of  $KV_6Sb_6$  and that  $KV_6Sb_6$  prepared from KH is not H-stabilized phase.

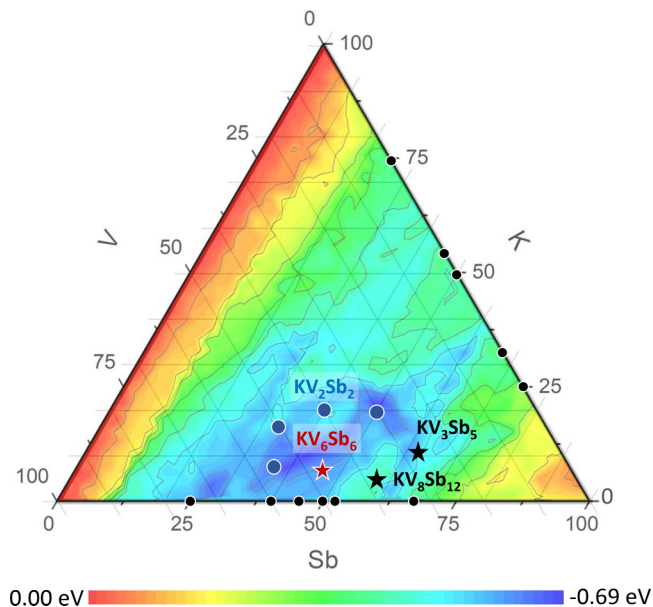


FIG. 2. Heat map for the K-V-Sb system. Ternary contour plot of formation energy as a function of compositions calculated using the machine learning approach [64,65]. The compositions denoted with black stars correspond to ternary compounds reported in the literature for A-V-Sb systems ( $A = K, Rb, Cs$ ) [29,50]. The composition denoted with a red star is the one discovered in this paper, and blue circles represent other attempted compositions.

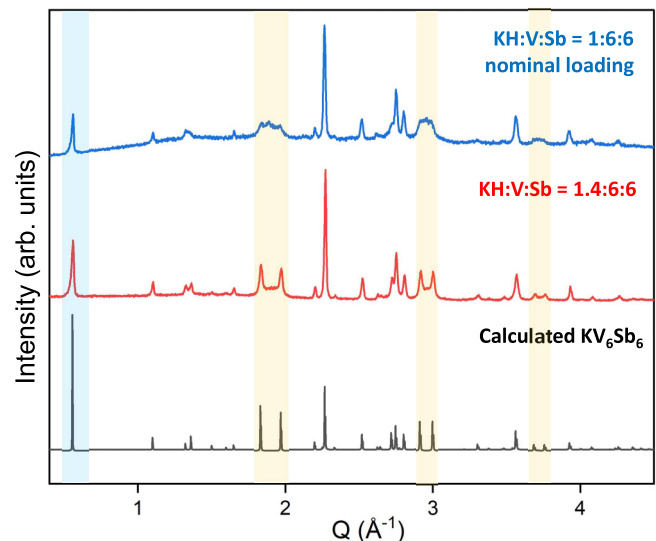


FIG. 3. Experimental powder x-ray diffraction pattern for sample synthesized with  $KH:V:Sb = 1.4:6:6$  and  $KH:V:Sb = 1:6:6$  loading molar ratio, signifying a difference in crystallinity with K content. The yellow shaded region highlights the difference in crystallinity for the set of two peaks, and the blue region highlights the preferred orientation.

Additionally, in our previous work on other alkali-metal-containing ternary antimonides, we saw no evidence of hydrogen incorporation when an alkali metal hydride was used as a precursor [61,63]. Nevertheless, the synthesis of  $KV_6Sb_6$  using elemental K results in a PXRD pattern with a well-resolved set of two peaks at  $Q \sim 1.8, 3,$  and  $3.7 \text{ \AA}^{-1}$  (Fig. S1(b) in the Supplemental Material [74]) compared with  $KV_6Sb_6$  synthesized using KH.

In summary, the hydride route in tandem with *in situ* studies and computationally predicted stable ternary compositions allowed for the optimization of synthesis conditions for fast synthesis of a high-purity polycrystalline sample of the title compound.

To further study the kinetics of the  $KV_6Sb_6$  formation using KH, we collected *in situ* high-temperature PXRD data upon heating of KH, V, and Sb powders mixed in a 1.3:6:6 molar ratio (Fig. 4). Initially, at RT, only diffraction peaks for Sb are seen in the PXRD data since Sb is the strongest x-ray scatterer of the three components (KH, V, and Sb). As the temperature approaches the melting point of Sb (903 K), diffraction peaks for V become visible at  $\sim 650$  K along with a simultaneous decrease in intensity of diffraction peaks for Sb, suggesting the onset of Sb melting. Further heating the mixture to 850 K promotes reaction of the starting elements, leading to the formation of  $VSb_2$  and  $KV_3Sb_5$ . This matches well with the synthesis temperature of 873 K for  $KV_3Sb_5$  [29]. There is no clear indication of the formation of K-Sb binaries in the given temperature range. Above 850 K,  $KV_3Sb_5$  transforms to  $KV_6Sb_6$ , with  $KV_6Sb_6$  becoming the major phase at 1073 K. It remains the major phase down to RT upon cooling. The temperature range over which the formation of the  $KV_6Sb_6$  occurs is in good agreement with the *in situ* study on the  $KV_3Sb_5$  compound (Fig. 1), supporting the earlier choice of synthesis temperature. The reaction is rapid because of the intimate mixing of precursors, allowing us to monitor reaction progress with *in situ* x-ray diffraction.  $KV_3Sb_5$  forms first at low temperatures and acts as an intermediate that transforms to  $KV_6Sb_6$  at higher temperatures. Based on the *in situ* study, the reaction mechanism can be roughly represented as  $KH + V + Sb \rightarrow VSb_2 + KV_3Sb_5 + \text{melt} \rightarrow KV_6Sb_6$ . Overall, the *in situ* study provided insights into the reaction mechanism and confirms the viability of utilizing KH for the synthesis of the  $KV_6Sb_6$  phase.

### B. Composition and thermal stability

Using EDX-SEM analysis, the composition of the phase was found to be  $K_{1.3(1)}V_{6.1(1)}Sb_{6.0(2)}$ , which is close to the composition of the compound obtained from PXRD data. Analysis was performed on a flat surface of an SPS-sintered pellet with 95% compactness. The sintering of the pellet for EDX-SEM analysis was accomplished under the same conditions as the pellet used for the measurement of transport properties (93% compactness). As evident from Fig. S3 in the Supplemental Material [74], sintering leads to a well-consolidated pellet and an even distribution of K, V, and Sb across the entire sample.

To study the thermal stability of  $KV_6Sb_6$ , *in situ* high-temperature synchrotron PXRD data were collected on a sample of  $KV_6Sb_6$  containing minor  $V_3Sb$  impurity in the

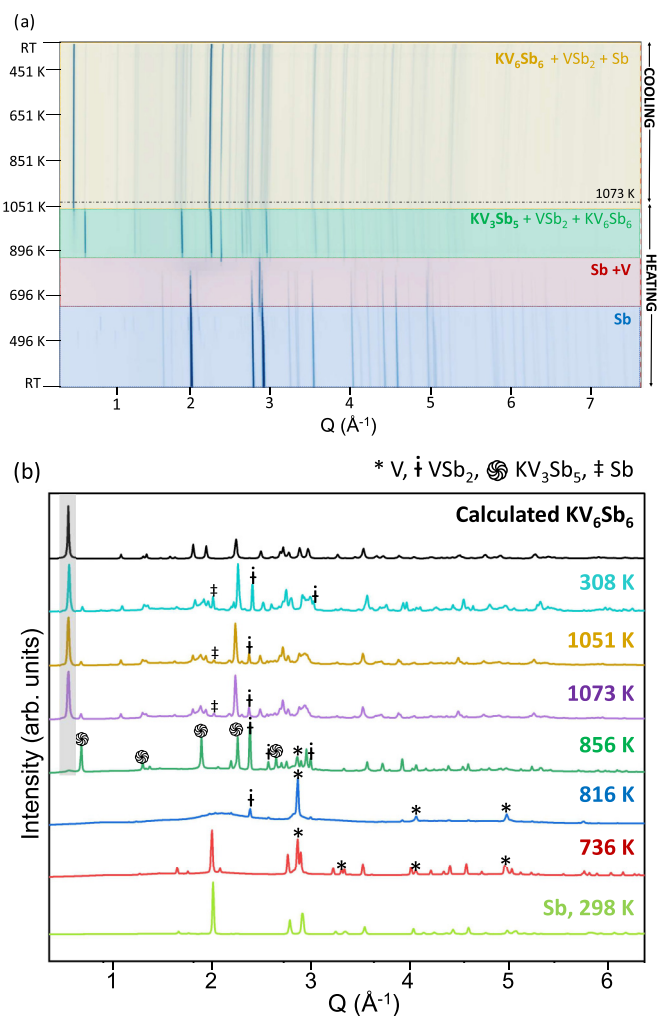


FIG. 4. (a) High-temperature *in situ* synchrotron powder x-ray diffraction (PXRD) data for the hydride reaction in the form of a waterfall plot displays sequential changes in the PXRD patterns, collected upon heating and cooling. Each vertical line represents a diffraction peak in the PXRD pattern. Distinct temperature ranges with the indicated phases present are highlighted in blue, red, green, and yellow. (b) Selected PXRD patterns showing the formation of  $KV_6Sb_6$  through the identified crystalline intermediates.

temperature range of RT to 1173 K (Fig. S4 in the Supplemental Material [74]). As seen in Fig. S4(a) in the Supplemental Material [74],  $KV_6Sb_6$  is thermally stable up to 1173 K. This is consistent with DSC data (Fig. S5 in the Supplemental Material [74]), as no thermal events were observed during the heating and cooling cycles. Figure S4(b) in the Supplemental Material [74] shows selected PXRD patterns from the *in situ* high-temperature synchrotron PXRD study, underlining the phase transformations over the temperature range.  $KV_6Sb_6$  is the major phase at all measured temperatures during the heating cycle. At  $\sim 500$  K during heating, the diffraction peaks of elemental Sb start to appear along with a slight increase in the intensity of diffraction peaks for the  $V_3Sb$ . We hypothesize that, upon heating, a small fraction of K is leached from the  $KV_6Sb_6$  phase due to a side reaction with the silica capillary (in which the sample is sealed), leading to the formation of  $V_3Sb$  and Sb. At  $\sim 773$  K, we see the simultaneous

appearance of the  $KV_3Sb_5$  phase and the disappearance of Sb and  $V_3Sb$ . This might be a result of the reaction between  $KV_6Sb_6$ ,  $V_3Sb$ , and Sb to form the comparatively Sb-rich  $KV_3Sb_5$  ternary phase. As the sample is heated  $> 1073$  K,  $KV_3Sb_5$  transforms back into  $KV_6Sb_6$ , in accordance with the findings of the *in situ* PXRD study for the  $KV_3Sb_5$  compound (Fig. 1) and the mechanistic study of the hydride reaction (Fig. 4). From the *in situ* studies, it can be concluded that the synthesis of  $KV_6Sb_6$  should be carried out at  $T \sim 1073$  K to avoid the formation of the competing ternary phase. Upon cooling, elemental Sb crystallizes at  $\sim 873$  K (m.p. 903 K), and the Sb fraction gradually increases as the sample is cooled to RT. In this paper, we indicate that  $KV_6Sb_6$  is thermally stable up to 1173 K.

To summarize, high-temperature *in situ* studies have been vital in the discovery and study of the  $KV_6Sb_6$  compound, first hinting at the existence of the title compound, then helping to pinpoint an appropriate synthesis temperature, offering insight into the reaction mechanism, and finally, in establishing the thermal stability of the compound.

### C. Crystal structure

Since hydride synthesis yields microcrystalline powders with crystals too small for single-crystal x-ray diffraction study, the crystal structure of the  $KV_6Sb_6$  phase was solved from high-resolution synchrotron PXRD data using FOX [71] and refined using JANA 2006 packages [72]. As described in the experimental part, indexing the peaks initially yielded a monoclinic  $C2/m$  unit cell, which on further refinement and analysis led to a rhombohedral  $R\bar{3}m$  model for the  $KV_6Sb_6$  compound. Parameters including lattice parameters, atomic coordinates, preferred orientation, site occupancy, and isotropic displacement parameters were refined. The calculated PXRD patterns for the two models were compared with the experimental HR-PXRD data for the phase (Fig. S6 in the Supplemental Material [74]). The two models closely resemble each other except for the splitting of certain peaks (Fig. S6 in the Supplemental Material [74]). Upon solving the structure of  $KV_6Sb_6$ , we became aware of the report on the isostructural compounds  $RbV_6Sb_6$  and  $CsV_6Sb_6$  [44–47]. The increase in the  $c$  parameter as the size of alkali metal cation increases ( $34.23$  Å for K,  $34.61$  Å for Rb, and  $35.28$  Å for Cs) follows the expected trend, while the variation in the  $a$  parameter [ $a(KV_6Sb_6) = 5.53$  Å,  $a(RbV_6Sb_6) = 5.51$  Å, and  $a(CsV_6Sb_6) = 5.51$  Å] is minor, leading to an overall increase in the unit cell volume. Careful analysis of the residual curve from the Rietveld refinement (Fig. S6(b) in the Supplemental Material [74]) indicated additional diffraction intensity between the (107) and (108) peaks at  $Q \sim 1.8$  Å<sup>-1</sup>, (207) and (208) at  $Q \sim 3.0$  Å<sup>-1</sup>, and (217) and (218) peaks at  $Q \sim 3.7$  Å<sup>-1</sup> (black arrows in Fig. S6(b) in the Supplemental Material [74]) as well as a positive difference between  $I_{obs} - I_{calc}$  for peaks with (003), (006), (0015), (110), and (1115)  $hkl$  indices (red arrows in Fig. S6(b) in the Supplemental Material [74]), resulting in relatively high  $R$  values for the fit. We hypothesize that the proposed rhombohedral model does not fully capture the complexity of the  $KV_6Sb_6$  structure. The deviations between experimental and refined PXRD patterns

could be attributed to the beginning of deintercalation of  $K^+$  ions from the layers to form a related  $K_{1-y}V_6Sb_6$  phase, as discussed earlier (Fig. S1 in the Supplemental Material [74] and Fig. 3) or could be due to inherent stacking faults in the layered structure that would cause discrepancies in diffraction intensity, leading to the unusual broadening of peaks even in the HR-PXRD data. Nonetheless, we believe that the  $R\bar{3}m$  model provides an acceptable fit of the PXRD data and is a plausible structural solution for the title compound.

The rhombohedral structure of the  $KV_6Sb_6$  compound consists of  $[V_6Sb_6]^-$  layers alternating with  $K^+$  layers (Fig. 5). There is one atomic site for K, one for V atoms, and three unique Sb atomic sites Sb(1), Sb(2), and Sb(3). A single  $[V_6Sb_6]$  layer can be represented as  $[Sb_2]-[V_3Sb]-[V_3Sb]-[Sb_2]$ , i.e., a double layer of  $[V_3Sb]$  capped by single layers of Sb atoms from either side [Fig. 5(a)]. Within the  $[V_6Sb_6]$  blocks, the Sb(1) and V atoms appear in the  $[V_3Sb]$  layers, whereas Sb(2) and Sb(3) atoms constitute the capping layers. V atoms in the structure form a Kagome network with a V-V distance of  $2.766$  Å, while the Sb(2) and Sb(3) atoms in the capping layers form a hexagonal network with Sb2-Sb3 distance of  $3.192$  Å [Fig. 5(b)]. The Sb(1) atoms are also arranged in a hexagonal pattern in the structure with an Sb1-Sb1 distance of  $5.532$  Å. Figure 5(d) shows the  $[V_6Sb_6]$  layer of  $KV_6Sb_6$ , highlighting the stacking of the V and Sb networks along the [001] direction. Layers are shifted with respect to one another as they stack along the [001] direction.

The structure of  $KV_6Sb_6$  displays remarkable similarities with the crystal structure of  $V_3Sb_2$ , a compound that also crystallizes in the rhombohedral space group  $R\bar{3}m$  [Figs. 6(a) and 6(b)]. The structure of the  $KV_6Sb_6$  ternary phase can be viewed as a derivative of the  $V_3Sb_2$  structure where two adjacent  $[V_3Sb]$  layers are stripped and replaced by a single layer of  $K^+$  [Figs. 6(a) and 6(b)]. The two compounds have identical  $[V_6Sb_6]$  layers [shaded in light blue in Figs. 6(a) and 6(b)]. The V atoms in both compounds are coordinated to Sb atoms to form a distorted square pyramid (Fig. S7 in the Supplemental Material [74]). Sb shows similar coordination environments in  $V_3Sb_2$  and  $KV_6Sb_6$  (Fig. S7 in the Supplemental Material [74]).

Figure 6 also illustrates how the structure of  $KV_6Sb_6$  is similar to that of  $KV_3Sb_5$  [29]. Both compounds have a layered structure. The  $KV_3Sb_5$  compound crystallizes in the hexagonal space group  $P6/mmm$  and hence has a more symmetric arrangement of atoms in the unit cell compared with  $KV_6Sb_6$ . This is also reflected in the change in the coordination environment of the V and the Sb atoms (Fig. S7 in the Supplemental Material [74]). The major difference between the two structures is the single layer of the V Kagome network in  $KV_3Sb_5$  as compared with the V Kagome bilayers in  $KV_6Sb_6$  and  $V_3Sb_2$ . In fact,  $KV_6Sb_6$  and  $KV_3Sb_5$  have similar layered structures with an extra layer of  $V_3Sb$  in  $KV_6Sb_6$  [Figs. 6(b) and 6(c)]. In summary,  $KV_6Sb_6$  has structural features strikingly similar to those of  $V_3Sb_2$  and  $KV_3Sb_5$ . Band structure calculations for  $KV_6Sb_6$  reported elsewhere [51,52] suggest a metallic behavior for the compound, which would mean that  $KV_6Sb_6$  is not a classical, charge-balanced Zintl phase [75,76].

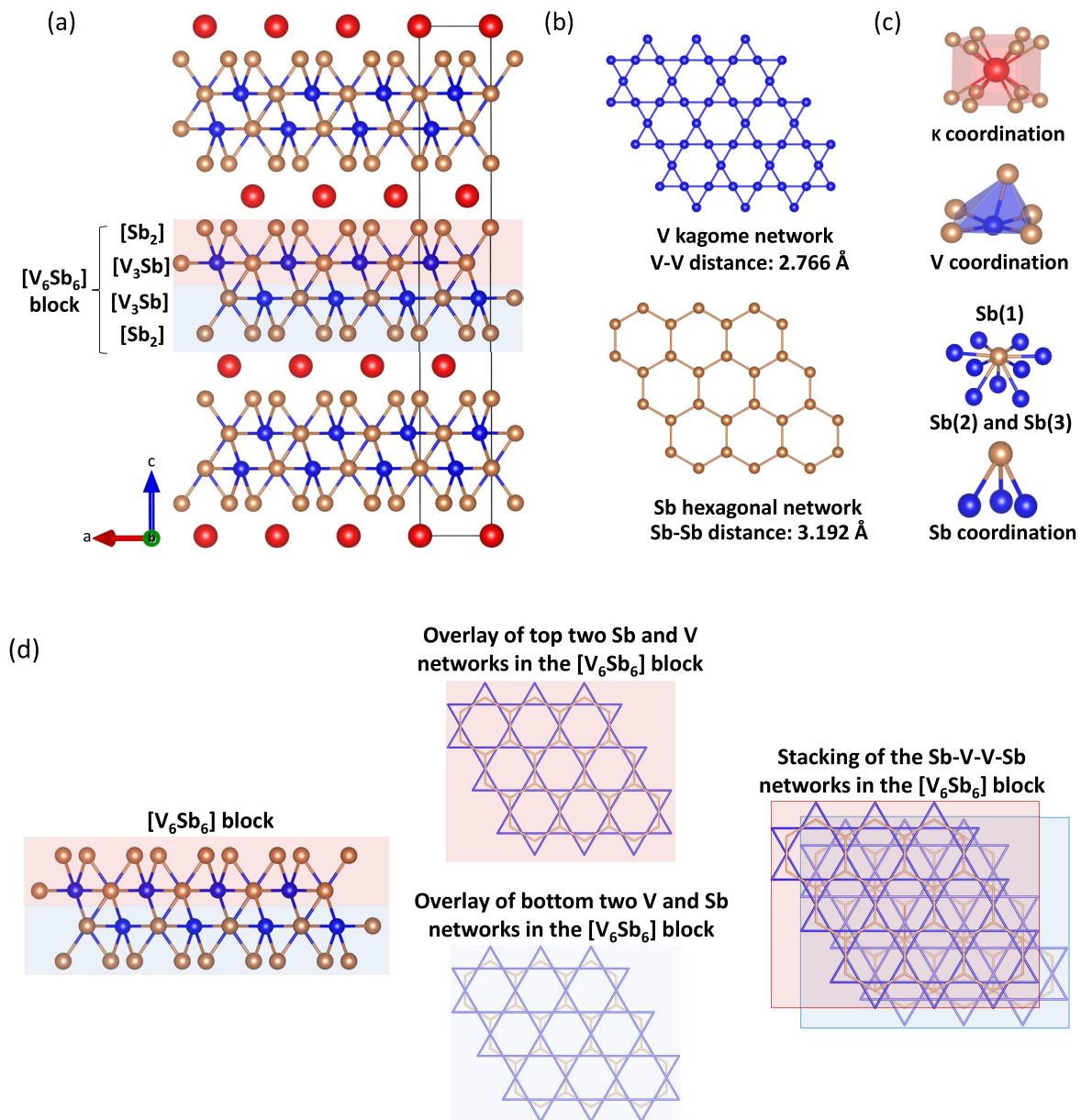


FIG. 5. Crystal structure of  $KV_6Sb_6$  [red: K, blue: V, and gold: Sb] highlighting (a) the layered structure, (b) V and Sb networks, (c) coordination environments of the K, V, and Sb atoms, and (d) stacking of Sb and V networks in the  $[V_6Sb_6]$  block.

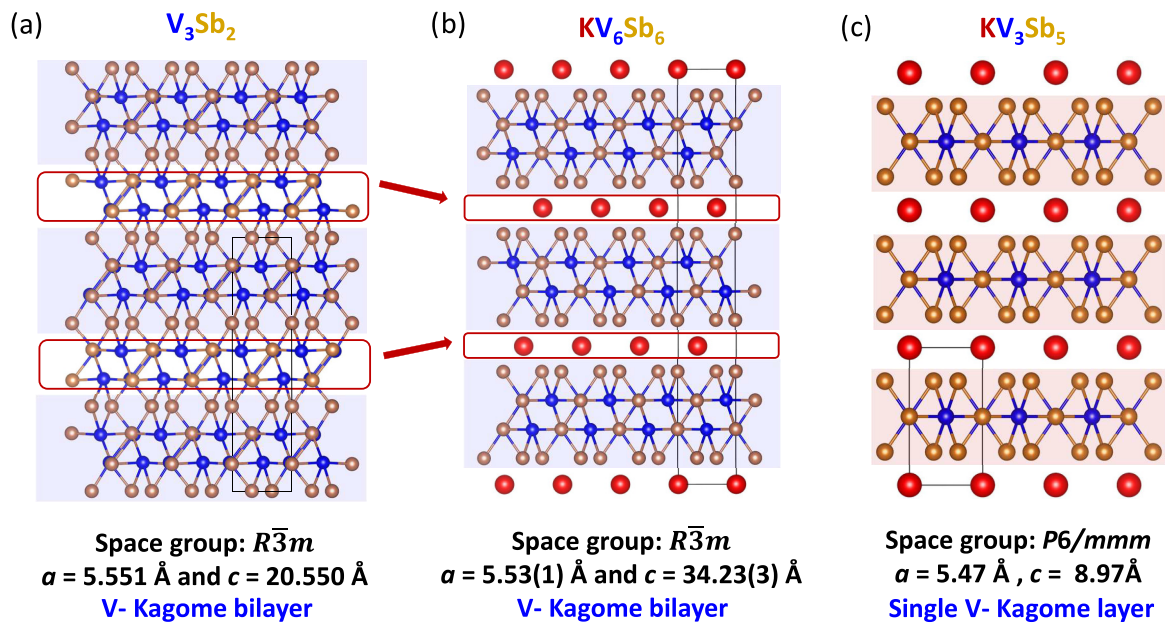
#### D. Magnetic and transport properties

As discussed in the previous section, the  $KV_6Sb_6$  compound is structurally similar to  $V_3Sb_2$  and  $KV_3Sb_5$  and features a Kagome lattice of V atoms. With the recent discovery of superconductivity in the  $AV_3Sb_5$  ( $A = K, Rb, Cs$ ) family of compounds [29–33], we examined the magnetic properties of  $KV_6Sb_6$ . Due to their structural similarities, we also compared the magnetic properties of  $KV_6Sb_6$  with those of  $V_3Sb_2$  and  $KV_3Sb_5$ .

Figure 7(a) represents a plot of molar dc magnetic susceptibility ( $\chi$ ) per V atom as a function of temperature for  $KV_6Sb_6$  and  $V_3Sb_2$ , measured at 0.1 T applied magnetic field. The data reveal temperature-independent (Pauli) paramagnetism for both  $KV_6Sb_6$  and  $V_3Sb_2$  with no splitting of the zero-field-cooling (ZFC) and field-cooling

(FC) curves. There is a slight upturn of magnetic moment at lower temperatures ( $T < 10$  K). The temperature dependence of  $\chi$  for  $KV_6Sb_6$  is similar to that of the isostructural  $RbV_6Sb_6$  and  $CsV_6Sb_6$  phases [50–53]. The paramagnetic behavior in  $KV_6Sb_6$  is evident from the linear trend of magnetization vs applied field for  $M(H)$ , collected at both 2 and 300 K [Fig. 7(b)]. The deviations from linearity in  $M(H)$  at 2 K for  $V_3Sb_2$  (Fig. S8 in the Supplemental Material [74]) suggest a ferromagnetic contribution, but given the small value of saturation magnetization, this feature is likely not intrinsic to the  $V_3Sb_2$  phase and might stem from ferromagnetic impurities. The magnetic susceptibility  $\chi$  per V atom is more than an order of magnitude higher for  $V_3Sb_2$  than for  $KV_6Sb_6$ . We found no evidence of superconductivity in  $KV_6Sb_6$  down to 2 K from either of these datasets or the



FIG. 6. Comparison of  $V_3Sb_2$ ,  $KV_6Sb_6$ , and  $KV_3Sb_5$  crystal structures.

ac susceptibility measurements (Fig. S9 in the Supplemental Material [74]). Even though  $AV_6Sb_6$  ( $A = K, Rb, Cs$ ) compounds are not superconducting at ambient pressure, superconductivity can be induced by applied hydrostatic pressures [ $T_{C,max}(KV_6Sb_6) = 0.37 \text{ K}$  at 31 GPa,  $T_{C,max}(RbV_6Sb_6) = 1.36 \text{ K}$  at 28 GPa, and  $T_{C,max}(CsV_6Sb_6) = 1.48 \text{ K}$  at 33 GPa] [52].

We also compared the low-temperature magnetic properties of the polycrystalline  $KV_3Sb_5$  sample synthesized via the hydride route with that of the polycrystalline  $KV_3Sb_5$  sample prepared via a traditional route from elements in the study by Ortiz *et al.* [29] (see Figs. S10 and S11 and discussion in the Supplemental Material [74]). Briefly, the magnetic properties of the  $KV_3Sb_5$  compound synthesized via the hydride route are consistent with the paramagnetic behavior and low magnetic moment per V atom previously observed [29]. The parameters of Curie-Weiss fit are consistent with the previous study [29], except for the Weiss constant. However, the anomaly at 80 K observed in both magnetization and heat-capacity measurements for the  $KV_3Sb_5$  sample synthesized via the traditional route from elements [29] is not seen for the  $KV_3Sb_5$  sample synthesized via the hydride route (Fig. S11 in the Supplemental Material [74]). The Curie-Weiss fit of the FC susceptibility curve for  $KV_6Sb_6$  shown in Fig. S12 in the Supplemental Material [74] reveals comparable values of the fit parameters for the  $KV_6Sb_6$  and  $KV_3Sb_5$  phases. Details of the fitting and the values of the parameters can be found in Fig. S12 in the Supplemental Material [74].

Given that  $KV_6Sb_6$  belongs to the family of ternary antimonides with a layered structure, we were interested in measuring the thermoelectric properties of  $KV_6Sb_6$ . Among the layered antimonides,  $AM_2Sb_2$  Zintl compounds ( $A = Ca, Sr, Ba, Eu, Yb$ ;  $M = Zn, Cd$ ) boast excellent thermoelectric properties [77–82]. Thermoelectric materials are characterized by the unitless figure of merit  $zT = S^2T/\rho\kappa$ , where  $S$  is the Seebeck coefficient,  $\rho$  is the electrical resistivity, and

$\kappa$  is the thermal conductivity. For decent thermoelectric performance,  $zT$  needs to be as high as possible and for practical applications should exceed 1 [83]. In the  $AM_2Sb_2$  family, the  $YbCd_2Sb_2$  compound has been reported to have  $zT = 1.0$  at 675 K [77,78]. The Mn-doped variants of  $YbCd_2Sb_2$  also display  $zT > 1$  in the moderate temperature range [78].

Measurements of low-temperature electrical and thermal transport properties of  $KV_6Sb_6$  (Figs. 8(a)–8(c)) were performed using an SPS-consolidated pellet with 93% compactness. Electrical resistivity  $\rho$  increases with an increase in temperature, indicating metallic behavior [Fig. 8(a)]. The values of  $\rho$  in the 5–300 K range ( $1.25 \times 10^{-5}$  to  $1.65 \times 10^{-5} \Omega m$ ) are typical for a metal. The resistivity reported earlier for the  $KV_6Sb_6$  phase in the same temperature range is  $0.25 \times 10^{-5}$  to  $0.45 \times 10^{-5} \Omega m$  [52], which is of the same order of magnitude as the resistivity values obtained in this paper. The  $\rho = \rho_0 + A_1T^2$  parabolic model provided a good fit of the resistivity data in the low-temperature range of 20–60 K, indicating that, at low temperatures, electron-electron scattering dominates. The model gave the value of parameter  $A_1 = 1.5 \times 10^{-10} \Omega m K^{-2}$  for  $KV_6Sb_6$  comparable with the  $A$  parameter of the  $KV_3Sb_5$  phase ( $3.0 \times 10^{-10} \Omega m K^{-2}$ ) [29]. In the higher-temperature range of 60–200 K, resistivity has a linear dependence on temperature. The data can be fit using the  $\rho = \rho_0 + A_2T$  model, in accordance with the electron-phonon scattering at high temperatures in a metal. We hypothesize that the upturn in resistivity  $< 20 \text{ K}$  is due to imperfections in the crystal structure, such as vacancies and stacking faults, since the resistivity measured on the flux-grown  $KV_6Sb_6$  single crystal lacks such a low-temperature feature [52].

The metallic nature of  $KV_6Sb_6$  is in line with the low values of the Seebeck coefficient  $S$ , which reaches  $8.5 \mu V K^{-1}$  at 300 K [Fig. 8(c)]. Positive values of  $S$  suggest holes as charge carriers. The total thermal conductivity ( $\kappa_{total}$ )

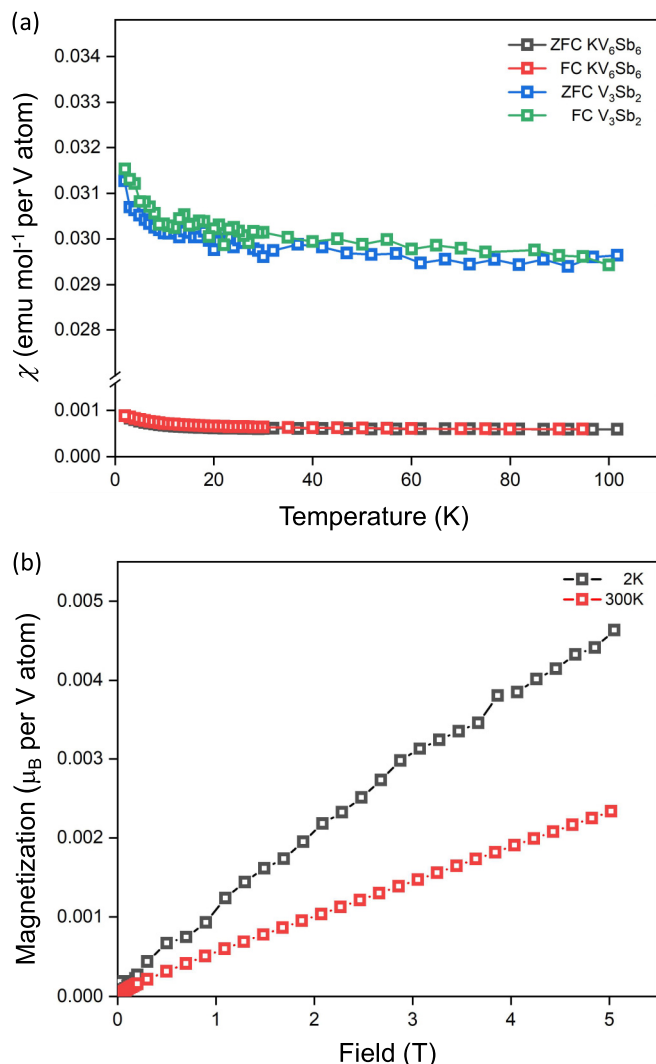


FIG. 7. Magnetic properties of the structurally related KV<sub>6</sub>Sb<sub>6</sub> and V<sub>3</sub>Sb<sub>2</sub> phases. (a) Zero-field-cooled (ZFC)/field-cooled (FC) magnetic susceptibility ( $\chi$ ) per V atom as a function of temperature for KV<sub>6</sub>Sb<sub>6</sub> and V<sub>3</sub>Sb<sub>2</sub> measured in the applied field of 0.1 T. (b) Magnetization per V atom for KV<sub>6</sub>Sb<sub>6</sub> as a function of magnetic field at 2 and 300 K.

for KV<sub>6</sub>Sb<sub>6</sub> is unusually low for a metallic compound and close to typical values for a glass (1.2 W K<sup>-1</sup> m<sup>-1</sup> at 300 K) [Fig. 8(b)]. The value of  $\kappa_{total}$  also resembles those for clathrates and layered antimonides studied for thermoelectric applications [79,83,84]. Electronic contribution to  $\kappa_{total}$  ( $\kappa_{el} = L\sigma T = LT/\rho$ ,  $L = 2.4 \times 10^{-8}$  W Ω K<sup>-2</sup>) is significant (~50% at 300 K), suggesting intrinsically low lattice thermal conductivity ( $\kappa_{lattice}$ ) for KV<sub>6</sub>Sb<sub>6</sub>. The comparison of thermal conductivity values at 300 K (Table I) shows that the  $\kappa_{total}$  of KV<sub>6</sub>Sb<sub>6</sub> is on par with other layered ternary antimonides. The figure of merit for the KV<sub>6</sub>Sb<sub>6</sub> compound  $zT$  is low (0.001 at 300 K), arising from the low Seebeck coefficient. With an intrinsically low  $\kappa$ , doping can be attempted to increase the  $S$  values of KV<sub>6</sub>Sb<sub>6</sub> to improve the thermoelectric performance. KV<sub>6</sub>Sb<sub>6</sub> has a layered structure with fairly independent ionic

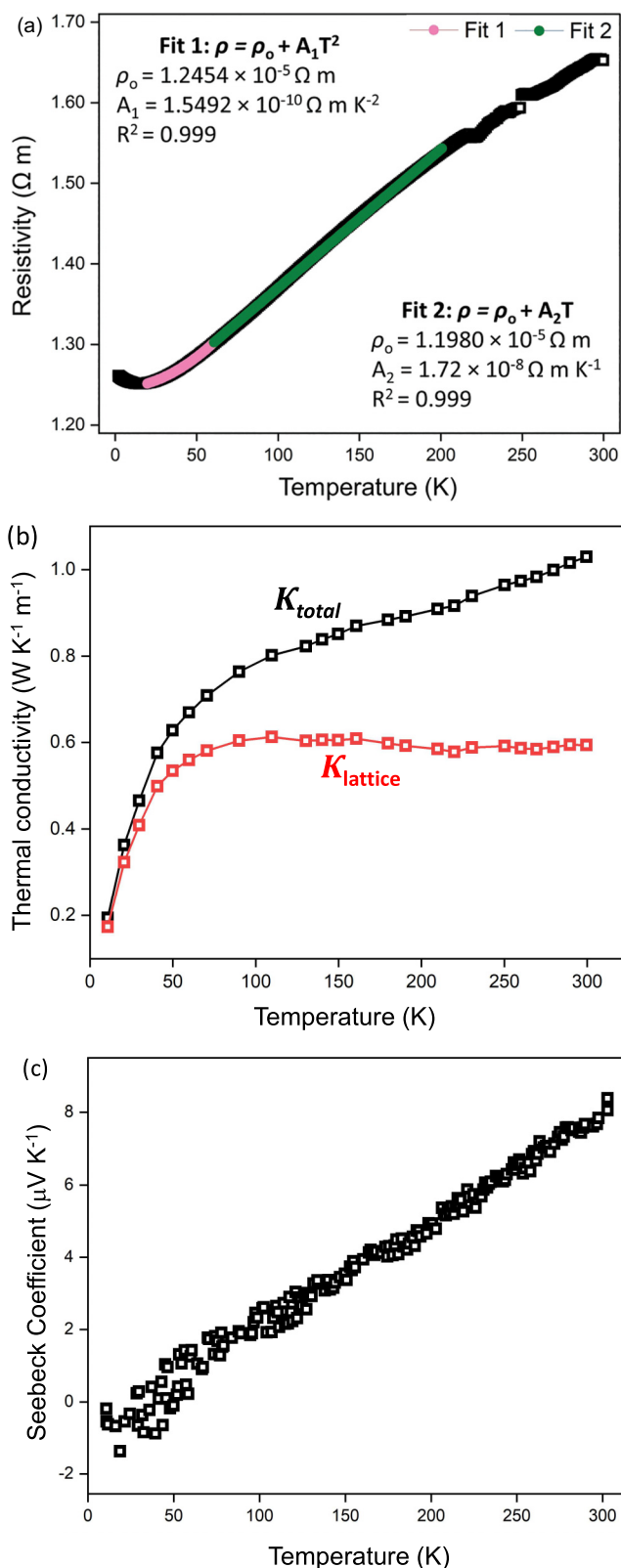


FIG. 8. Transport properties of KV<sub>6</sub>Sb<sub>6</sub> phases as a function of temperature. (a) Electrical resistivity  $\rho$ , (b) thermal conductivity  $\kappa$ , and (c) Seebeck coefficient  $S$ . The variation in resistivity in the 200–250 K range is not due to a phase transition but is attributed to the loose electrical contact.

TABLE I. Total thermal conductivity ( $\kappa_{\text{total}}$ ) and RT figure of merit  $zT$  for some layered antimonides.

Compound	$\kappa_{\text{total}}$ at 300 K ( $\text{W K}^{-1} \text{m}^{-1}$ )	$zT$ at 300 K
KV <sub>6</sub> Sb <sub>6</sub> (This paper)	1.00	0.001
Mg <sub>3</sub> Sb <sub>2</sub> [80]	1.35	0.002
YbCd <sub>2</sub> Sb <sub>2</sub> [77,78]	2.20	0.145
EuCd <sub>2</sub> Sb <sub>2</sub> [77]	1.35	0.125
CaZn <sub>2</sub> Sb <sub>2</sub> [81]	2.20	0.075
YbCd <sub>1.6</sub> Mn <sub>0.4</sub> Sb <sub>2</sub> [78]	1.10	0.140
Ca <sub>0.5</sub> Yb <sub>0.5</sub> Zn <sub>2</sub> Sb <sub>2</sub> [82]	1.00	0.100

(K<sup>+</sup> layers) and covalent fragments (V<sub>6</sub>Sb<sub>6</sub> layers), potentially allowing for the alteration of the electronic structure via doping to improve the TE properties. Moreover, the high-temperature thermoelectric properties of KV<sub>6</sub>Sb<sub>6</sub> should be a subject of future investigation given the exceptional thermal stability of KV<sub>6</sub>Sb<sub>6</sub> up to  $\sim 1173$  K.

#### IV. CONCLUSIONS

The hydride synthesis route guided by *in situ* PXRD and computationally predicted stable compositions in the K-V-Sb system led to the discovery of the KV<sub>6</sub>Sb<sub>6</sub> phase. *In situ* PXRD study highlighted the thermal stability of the compound up to 1173 K. Additionally, *in situ* study aided the elucidation of the reaction mechanism when using a hydride precursor. The formation of the title compound proceeds via the formation of the intermediate ternary KV<sub>3</sub>Sb<sub>5</sub>, which eventually transforms to KV<sub>6</sub>Sb<sub>6</sub> upon further heating. The KV<sub>6</sub>Sb<sub>6</sub> compound is isostructural to RbV<sub>6</sub>Sb<sub>6</sub> and CsV<sub>6</sub>Sb<sub>6</sub> phases and crystallizes in a  $R\bar{3}m$  layered structure that consists of alternating K<sup>+</sup> and [V<sub>6</sub>Sb<sub>6</sub>] layers. Within the [V<sub>6</sub>Sb<sub>6</sub>] layer, V atoms form Kagome bilayers, while Sb atoms form a graphenelike hexagonal net. PXRD data indicate a clear tendency for K to move out of the layers, altering the PXRD pattern and making this compound a candidate for deintercalation studies to further alter its transport properties. The KV<sub>6</sub>Sb<sub>6</sub> compound displays temperature-independent paramagnetic behavior and lacks superconductivity  $> 2$  K at ambient pressure, like the Rb and Cs analogs. KV<sub>6</sub>Sb<sub>6</sub> is

metallic, with low positive values of Seebeck coefficient and intrinsically low total thermal conductivity of  $1.0 \text{ W K}^{-1} \text{ m}^{-1}$  at 300 K. Doping or K<sup>+</sup> ions deintercalation from the KV<sub>6</sub>Sb<sub>6</sub> crystal structure can pave the way for optimized thermoelectric properties by modification of its electronic structure.

Through this paper, we have expanded the family of Kagome compounds in the A-V-Sb system by utilizing compositional screening via hydride synthesis. Hydride synthesis presents an alternative method for the preparation of ternary compounds in the K-V-Sb and similar systems, offering advantages such as thorough mixing of precursors to overcome diffusion barriers, lower synthesis temperature, and shorter synthesis time. Hydride synthesis combined with *in situ* diffraction and machine learning capabilities to rapidly optimize reaction temperatures and composition offers an effective strategy for the discovery of compounds with potentially remarkable properties and can be extended toward other systems with early 3d transition metals.

#### ACKNOWLEDGMENTS

Financial support from the National Science Foundation (U.S.) Division of Materials Research (DMR-1944551) CAREER Award is gratefully acknowledged. The magnetic measurements were supported by the Division of Materials Science and Engineering of the Office of Basic Energy Sciences, Office of Science of the U.S. Department of Energy through the Ames National Laboratory. Ames National Laboratory is operated for the DOE by Iowa State University under Contract No. DE-AC02-07CH11358. Use of the Advanced Photon Source at Argonne National Laboratory was supported by the U.S. Department of Energy, Office of Science, Office of Basic Energy Sciences, under Contract No. DE-AC02-06CH11357. Dr. W. Xu and Dr. A. Yakovenko at 17-BM are acknowledged for helping with high-temperature synchrotron PXRD data collection and Dr. S. Lapidus at 11-BM beamline APS ANL for the help with HR-PXRD data collection. We thank Dr. K. Kovnir (Chemistry Department, Iowa State University, and DOE Ames Laboratory) for the access to DSC-TG and PPMS and Dr. Warren Straszheim (Materials Analysis Research Laboratory, Iowa State University) for the help with SEM/EDXS data acquisition.

- 
- [1] S. K. Pati and C. N. R. Rao, Kagome network compounds and their novel magnetic properties, *Chem. Commun.* **4683** (2008).
- [2] M. Jovanovic and L. M. Schoop, Simple chemical rules for predicting band structures of Kagome materials, *J. Am. Chem. Soc.* **144**, 10978 (2022).
- [3] V. Meschke, P. Gorai, V. Stevanovic, and E. S. Toberer, Search and structural featurization of magnetically frustrated Kagome lattices, *Chem. Mater.* **33**, 4373 (2021).
- [4] J. R. Chamorro, T. M. McQueen, and T. T. Tran, Chemistry of quantum spin liquids, *Chem. Rev.* **121**, 2898 (2020).
- [5] L. Balents, Spin liquids in frustrated magnets, *Nature (London)* **464**, 199 (2010).
- [6] M. Sinha, H. K. Vivanco, C. Wan, M. A. Siegler, V. J. Stewart, E. A. Pogue, L. A. Pressley, T. Berry, Z. Wang, I. Johnson *et al.*, Twisting of 2D Kagomé sheets in layered intermetallics, *ACS Cent. Sci.* **7**, 1381 (2021).
- [7] M. R. Norman, Colloquium: Herbertsmithite and the search for the quantum spin liquid, *Rev. Mod. Phys.* **88**, 041002 (2016).
- [8] S. Lucile and L. Balents, Quantum spin liquids: A review, *Rep. Prog. Phys.* **80**, 016502 (2016).
- [9] J. E. Greedan, Geometrically frustrated magnetic materials, *J. Mater. Chem.* **11**, 37 (2001).
- [10] D. Grohol, D. G. Nocera, and D. Papoutsakis, Magnetism of pure iron jarosites, *Phys. Rev. B* **67**, 064401 (2003).

- [11] C. N. R. Rao, E. V. Sampathkumaran, R. Nagarajan, G. Paul, J. N. Behera, and A. Choudhury, Synthesis, structure, and the unusual magnetic properties of an amine-templated iron (II) sulfate possessing the Kagome lattice, *Chem. Mater.* **16**, 1441 (2004).
- [12] D. G. Nocera, B. M. Bartlett, D. Grohol, D. Papoutsakis, and M. P. Shores, Spin frustration in 2D Kagomé lattices: A problem for inorganic synthetic chemistry, *Chem. Eur. J.* **10**, 3850 (2004).
- [13] R. A. Klein, J. P. S. Walsh, S. M. Clarke, Y. Guo, W. Bi, G. Fabbri, Y. Meng, D. Haskel, E. E. Alp, R. P. Van Duyne *et al.*, Impact of pressure on magnetic order in jarosite, *J. Am. Chem. Soc.* **140**, 12001 (2018).
- [14] R. A. Klein, J. P. S. Walsh, S. M. Clarke, Z. Liu, E. E. Alp, W. Bi, Y. Meng, A. B. Altman, P. Chow, Y. Xiao *et al.*, Pressure-induced collapse of magnetic order in jarosite, *Phys. Rev. Lett.* **125**, 077202 (2020).
- [15] M. A. Subramanian, G. Aravamudan, and G. V. Subba Rao, Oxide pyrochlores—A review, *Prog. Solid State Chem.* **15**, 55 (1983).
- [16] M. P. Zinkin, M. J. Harris, and T. Zeiske, Short-range magnetic order in the frustrated pyrochlore antiferromagnet CsNiCrF<sub>6</sub>, *Phys. Rev. B* **56**, 11786 (1997).
- [17] M. Enjalran, M. J. P. Gingras, Y. J. Kao, A. Del Maestro, and H. R. Molavian, The spin liquid state of the Tb<sub>2</sub>Ti<sub>2</sub>O<sub>7</sub> pyrochlore antiferromagnet: A puzzling state of affairs, *J. Phys.: Condens. Matter* **16**, S673 (2004).
- [18] R. Moessner and A. P. Ramirez, Geometrical frustration, *Phys. Today* **59**(2), 24 (2006).
- [19] M. P. Shores, E. A. Nytko, B. M. Bartlett, and D. G. Nocera, A structurally perfect  $S = \frac{1}{2}$  Kagomé antiferromagnet, *J. Am. Chem. Soc.* **127**, 13462 (2005).
- [20] R. Sibille, E. Lhotel, M. C. Hatnean, G. Balakrishnan, B. Fåk, N. Gauthier, T. Fennell, and M. Kenzelmann, Candidate quantum spin ice in the pyrochlore Pr<sub>2</sub>Hf<sub>2</sub>O<sub>7</sub>, *Phys. Rev. B* **94**, 024436 (2016).
- [21] L. Opherden, J. Hornung, T. Herrmannsdörfer, J. Xu, A. T. M. N. Islam, B. Lake, and J. Wosnitza, Evolution of antiferromagnetic domains in the all-in-all-out ordered pyrochlore Nd<sub>2</sub>Zr<sub>2</sub>O<sub>7</sub>, *Phys. Rev. B* **95**, 184418 (2017).
- [22] J. D. Thompson, P. A. McClarty, D. Prabhakaran, I. Cabrera, T. Guidi, and R. Coldea, Quasiparticle breakdown and spin Hamiltonian of the frustrated quantum pyrochlore Yb<sub>2</sub>Ti<sub>2</sub>O<sub>7</sub> in a magnetic field, *Phys. Rev. Lett.* **119**, 057203 (2017).
- [23] T. A. Bojesen and S. Onoda, Quantum spin ice under a [111] magnetic field: From pyrochlore to Kagome, *Phys. Rev. Lett.* **119**, 227204 (2017).
- [24] E. Lhotel, S. Petit, M. Ciomaga Hatnean, J. Ollivier, H. Mutka, E. Ressouche, M. R. Lees, and G. Balakrishnan, Evidence for dynamic Kagome ice, *Nat. Commun.* **9**, 3786 (2018).
- [25] R. S. W. Braithwaite, K. Mereiter, W. H. Paar, and A. M. Clark, Herbertsmithite, Cu<sub>3</sub>Zn(OH)<sub>6</sub>Cl<sub>2</sub>, a new species, and the definition of paratacamite, *Mineral. Mag.* **68**, 527 (2004).
- [26] K. Zhao, H. Deng, H. Chen, K. A. Ross, V. Petříček, G. Günther, M. Russina, V. Hutnanu, and P. Gegenwart, Realization of the Kagome spin ice state in a frustrated intermetallic compound, *Science* **367**, 1218 (2020).
- [27] Z. Wang, H. Zhao, M. Lyu, J. Xiang, Y. Isikawa, S. Zhang, and P. Sun, Frustrated antiferromagnetism and heavy-fermion-like behavior in PrPdAl, *Phys. Rev. B* **105**, 125113 (2022).
- [28] H. Ge, L. Zhang, N. Zhao, J. Yang, L. Wang, L. Zhou, Y. Fu, T. T. Li, Z. M. Song, F. Ding *et al.*, Successive magnetic orderings in the Ising spin chain magnet DyNi<sub>5</sub>Ge<sub>3</sub>, *Phys. Rev. Mater.* **6**, 085001 (2022).
- [29] B. R. Ortiz, L. C. Gomes, J. R. Morey, M. Winiarski, M. Bordelon, J. S. Mangum, I. W. H. Oswald, J. A. Rodriguez-Rivera, J. R. Neilson, S. D. Wilson *et al.*, New Kagome prototype materials: Discovery of KV<sub>3</sub>Sb<sub>5</sub>, RbV<sub>3</sub>Sb<sub>5</sub>, and CsV<sub>3</sub>Sb<sub>5</sub>, *Phys. Rev. Mater.* **3**, 094407 (2019).
- [30] B. R. Ortiz, P. M. Sarte, E. M. Kenney, M. J. Graf, S. M. L. Teicher, R. Seshadri, and S. D. Wilson, Superconductivity in the Z<sub>2</sub> Kagome metal KV<sub>3</sub>Sb<sub>5</sub>, *Phys. Rev. Mater.* **5**, 034801 (2021).
- [31] Y. Qiangwei, Z. Tu, C. Gong, Y. Fu, S. Yan, and H. Lei, Superconductivity and normal-state properties of Kagome metal RbV<sub>3</sub>Sb<sub>5</sub> single crystals, *Chin. Phys. Lett.* **38**, 037403 (2021).
- [32] B. R. Ortiz, S. M. L. Teicher, Y. Hu, J. L. Zuo, P. M. Sarte, E. C. Schueller, A. M. M. Abeykoon, M. J. Krogstad, S. Rosenkranz, R. Osborn *et al.*, CsV<sub>3</sub>Sb<sub>5</sub>: A Z<sub>2</sub> topological Kagome metal with a superconducting ground state, *Phys. Rev. Lett.* **125**, 247002 (2020).
- [33] K. Jiang, T. Wu, J. X. Yin, Z. Wang, M. Z. Hasan, S. D. Wilson, X. Chen, and J. Hu, Kagome superconductors AV<sub>3</sub>Sb<sub>5</sub> (A = K, Rb, Cs), *Nat. Sci. Rev.* **10**, 199 (2023).
- [34] T. Neupert, M. M. Denner, J. X. Yin, R. Thomale, and M. Z. Hasan, Charge order and superconductivity in Kagome materials, *Nat. Phys.* **18**, 137 (2022).
- [35] C. Hui, B. Hu, Y. Ye, H. Yang, and H. Gao, Superconductivity and unconventional density waves in vanadium-based Kagome materials AV<sub>3</sub>Sb<sub>5</sub>, *Chin. Phys. B* **31**, 097405 (2022).
- [36] T. Rina, Y. Yamakawa, S. Onari, and H. Kontani, Mechanism of exotic density-wave and beyond-Migdal unconventional superconductivity in Kagome metal AV<sub>3</sub>Sb<sub>5</sub> (A = K, Rb, Cs), *Sci. Adv.* **8**, 4108 (2022).
- [37] L. Hailan, Q. Gao, H. Liu, Y. Gu, D. Wu, C. Yi, J. Jia, S. Wu, X. Luo, Y. Xu *et al.*, Electronic nature of charge density wave and electron-phonon coupling in Kagome superconductor KV<sub>3</sub>Sb<sub>5</sub>, *Nat. Commun.* **13**, 273 (2022).
- [38] Y. X. Jiang, X. Y. Yin, M. M. Denner, N. Shumiya, B. R. Ortiz, G. Xu, Z. Guguchia, J. He, M. D. Hossain, X. Liu *et al.*, Unconventional chiral charge order in Kagome superconductor KV<sub>3</sub>Sb<sub>5</sub>, *Nat. Mater.* **20**, 1353 (2021).
- [39] Y. M. Oey, F. Kaboudvand, B. R. Ortiz, R. Seshadri, and S. D. Wilson, Tuning charge-density wave order and superconductivity in the Kagome metals KV<sub>3</sub>Sb<sub>[5-x]</sub>Sn<sub>x</sub> and RbV<sub>3</sub>Sb<sub>[5-x]</sub>Sn<sub>x</sub>, *Phys. Rev. Mater.* **6**, 074802 (2022).
- [40] M. Liu, T. Han, X. Hu, Y. Tu, Z. Zhang, M. Long, X. Hou, Q. Mu, and L. Shan, Evolution of superconductivity and charge density wave through Ta and Mo doping in CsV<sub>3</sub>Sb<sub>5</sub>, *Phys. Rev. B* **106**, L140501 (2022).
- [41] Y. Li, Q. Li, X. Fan, J. Liu, Q. Feng, M. Liu, C. Wang, J. X. Yin, J. Duan, X. Li *et al.*, Tuning the competition between superconductivity and charge order in the Kagome superconductor Cs(V<sub>1-x</sub>Nb<sub>x</sub>)<sub>3</sub>Sb<sub>5</sub>, *Phys. Rev. B* **105**, L180507 (2022).
- [42] Y. Liu, Y. Wang, Y. Cai, Z. Hao, X. M. Ma, L. Wang, C. Liu, J. Chen, L. Zhou, J. Wang *et al.*, Doping evolution of superconductivity, charge order and band topology in hole-doped

- topological Kagome superconductors  $\text{Cs}(\text{V}_{1-x}\text{Ti}_x)_3\text{Sb}_5$ , *Phys. Rev. Mater.* **7**, 064801 (2023).
- [43] Y. M. Oey, B. R. Ortiz, F. Kaboudvand, J. Frassinetti, E. Garcia, R. Cong, S. Sanna, V. F. Mitrović, R. Seshadri, and S. D. Wilson, Fermi level tuning and double-dome superconductivity in the Kagome metal  $\text{CsV}_3\text{Sb}_{5-x}\text{Sn}_x$ , *Phys. Rev. Mater.* **6**, L041801 (2022).
- [44] D. Werhahn, B. R. Ortiz, A. K. Hay, S. D. Wilson, R. Seshadri, and D. Johrendt, The Kagomé metals  $\text{RbTi}_3\text{Bi}_5$  and  $\text{CsTi}_3\text{Bi}_5$ , *Z. Naturforschung, B* **77**, 757 (2022).
- [45] Y. Wang, Y. Liu, Z. Hao, W. Cheng, J. Deng, Y. Wang, Y. Gu, X. M. Ma, H. Rong, F. Zhang *et al.*, Flat band and  $Z_2$  topology of Kagome metal  $\text{CsTi}_3\text{Bi}_5$ , *Chin. Phys. Lett.* **40**, 037102 (2023).
- [46] H. Yang, Z. Zhao, X. W. Yi, J. Liu, J. Y. You, Y. Zhang, H. Guo, X. Lin, C. Shen, H. Chen *et al.*, Titanium-based Kagome superconductor  $\text{CsTi}_3\text{Bi}_5$  and topological states, [arXiv:2209.03840](https://arxiv.org/abs/2209.03840).
- [47] Y. Hu, C. Le, Y. Zhang, Z. Zhao, J. Liu, J. Ma, N. C. Plumb, M. Radovic, H. Chen, A. P. Schnyder *et al.*, Non-trivial band topology and orbital-selective electronic nematicity in a new titanium-based Kagome superconductor, *Nat. Phys.* (2023).
- [48] X. Chen, X. Liu, W. Xia, X. Mi, L. Zhong, K. Yang, L. Zhang, Y. Gan, Y. Liu, G. Wang *et al.*, Electrical and thermal transport properties of Kagome metals  $\text{ATi}_3\text{Bi}_5$  ( $A = \text{Rb}, \text{Cs}$ ), *Phys. Rev. B* **107**, 174510 (2023).
- [49] Y. Zhou, L. Chen, X. Ji, C. Liu, K. Liao, Z. Guo, J. O. Wang, H. Weng, and G. Wang, Physical properties, electronic structure, and strain-tuned monolayer of the weak topological insulator  $\text{RbTi}_3\text{Bi}_5$  with Kagome lattice, [arXiv:2301.01633](https://arxiv.org/abs/2301.01633).
- [50] Y. Yang, W. Fan, Q. Zhang, Z. Chen, X. Chen, T. Ying, X. Wu, X. Yang, F. Meng, G. Li *et al.*, Discovery of two families of VSb-based compounds with V-Kagome lattice, *Chin. Phys. Lett.* **38**, 127102 (2021).
- [51] Y. Yang, R. Wang, M. Z. Shi, Z. Wang, Z. Xiang, and X. H. Chen, Type-II nodal line fermions in the  $Z_2$  topological semimetals  $\text{AV}_6\text{Sb}_6$  ( $A = \text{K}, \text{Rb}, \text{and Cs}$ ) with a Kagome bilayer, *Phys. Rev. B* **104**, 245128 (2021).
- [52] M. Shi, F. Yu, Y. Yang, F. Meng, B. Lei, Y. Luo, Z. Sun, J. He, R. Wang, Z. Jiang *et al.*, A new class of bilayer Kagome lattice compounds with Dirac nodal lines and pressure-induced superconductivity, *Nat. Commun.* **13**, 2773 (2022).
- [53] Q. Yin, Z. Tu, C. Gong, S. Tian, and H. Lei, Structures and physical properties of V-based Kagome metals  $\text{CsV}_6\text{Sb}_6$  and  $\text{CsV}_8\text{Sb}_{12}$ , *Chin. Phys. Lett.* **38**, 127401 (2021).
- [54] K. Kovnir, Predictive synthesis, *Chem. Mater.* **33**, 4835 (2021).
- [55] M. G. Kanatzidis, Discovery-synthesis, design, and prediction of chalcogenide phases, *Inorg. Chem.* **56**, 3158 (2017).
- [56] D. L. M. Cordova and D. C. Johnson, Synthesis of metastable inorganic solids with extended structures, *Chem. Phys. Chem.* **21**, 1345 (2020).
- [57] X. Ma, F. Xu, T. M. Atkins, A. M. Goforth, D. Neiner, A. Navrotsky, and S. M. Kauzlarich, A versatile low temperature synthetic route to Zintl phase precursors:  $\text{Na}_4\text{Si}_4$ ,  $\text{Na}_4\text{Ge}_4$  and  $\text{K}_4\text{Ge}_4$  as examples, *Dalton Trans.* **46**, 10250 (2009).
- [58] J. V. Zaikina, M. Batuk, A. M. Abakumov, A. Navrotsky, and S. M. Kauzlarich, Facile synthesis of  $\text{Ba}_{1-x}\text{K}_x\text{Fe}_2\text{As}_2$  superconductors via hydride route, *J. Am. Chem. Soc.* **136**, 16932 (2014).
- [59] V. Gvozdetzkyi, M. P. Hanrahan, R. A. Ribeiro, T. H. Kim, L. Zhou, A. J. Rossini, P. C. Canfield, and J. V. Zaikina, A hydride route to ternary alkali metal borides: A case study of lithium nickel borides, *Chem. Eur. J.* **25**, 4123 (2019).
- [60] V. Gvozdetzkyi, G. Bhaskar, M. Batuk, X. Zhao, R. Wang, S. L. Carnahan, M. P. Hanrahan, R. A. Ribeiro, P. C. Canfield, A. J. Rossini *et al.*, Computationally driven discovery of a family of layered LiNiB polymorphs, *Angew. Chem. Int. Ed.* **58**, 15855 (2019).
- [61] T. Cox, V. Gvozdetzkyi, B. Owens-Baird, and J. V. Zaikina, Rapid phase screening via hydride route: A discovery of  $\text{K}_{8-x}\text{Zn}_{18+3x}\text{Sb}_{16}$ , *Chem. Mater.* **30**, 8707 (2018).
- [62] A. N. Adeyemi, G. Bhaskar, T. Cox, S. Hong, V. Gvozdetzkyi, and J. V. Zaikina, *Hydride Precursors in Materials Synthesis, Comprehensive Inorganic Chemistry III*, 3<sup>rd</sup> ed. (Elsevier, City, 2023), p. 128.
- [63] V. Gvozdetzkyi, B. Owens-Baird, S. Hong, T. Cox, G. Bhaskar, C. Harmer, Y. Sun, F. Zhang, C. Z. Wang, K. M. Ho *et al.*, From  $\text{NaZn}_4\text{Sb}_3$  to  $\text{HT-Na}_{1-x}\text{Zn}_{4-y}\text{Sb}_3$ : Panoramic hydride synthesis, structural diversity, and thermoelectric properties, *Chem. Mater.* **31**, 8695 (2019).
- [64] <http://info.eecs.northwestern.edu/FEpredictor>.
- [65] B. Meredig, A. Agrawal, S. Kirklin, J. E. Saal, J. W. Doak, A. Thompson, K. Zhang, A. Choudhary, and C. Wolverton, Combinatorial screening for new materials in unconstrained composition space with machine learning, *Phys. Rev. B* **89**, 094104 (2014).
- [66] D. W. Rudd, D. W. Vose, and S. Johnson, The permeability of niobium to hydrogen, *J. Phys. Chem.* **66**, 351 (1962).
- [67] R. E. Buxbaum and A. B. Kinney, Hydrogen transport through tubular membranes of palladium-coated tantalum and niobium, *Ind. Eng. Chem. Res.* **35**, 530 (1996).
- [68] H. Yukawa, T. Nambu, Y. Matsumoto, N. Watanabe, G. Zhang, and M. Morinaga, Alloy design of Nb-based hydrogen permeable membrane with strong resistance to hydrogen embrittlement, *Mater. Trans.* **49**, 2202 (2008).
- [69] Match! - Phase Analysis using Powder Diffraction, Version 3.x, Crystal Impact - Dr. H. Putz & Dr. K. Brandenburg GbR, Kreuzherrenstr. 102, 53227 Bonn, Germany, <https://www.crystalimpact.de/match>.
- [70] P. J. Chupas, K. W. Chapman, C. Kurtz, J. C. Hanson, P. L. Lee, and C. P. Grey, A versatile sample-environment cell for non-ambient x-ray scattering experiments, *J. Appl. Crystallogr.* **41**, 822 (2008).
- [71] V. Favre-Nicolin and R. Černý, FOX, free objects for crystallography: A modular approach to *ab initio* structure determination from powder diffraction, *J. Appl. Crystallogr.* **35**, 734 (2002).
- [72] V. Petricek, M. Dusek, and L. Palatinus, Crystallographic Computing System JANA2006: General features, *Z. Kristallogr.* **229**, 345 (2014).
- [73] A. L. Spek, Structure validation in chemical crystallography, *Acta Cryst. D* **65**, 148 (2009).
- [74] See Supplemental Material at <http://link.aps.org/supplemental/10.1103/PhysRevMaterials.7.115002> for description of the effect of synthesis with varying molar quantities of KH and K on the phase purity of  $\text{KV}_6\text{Sb}_6$ ; confirmation of the preferred orientation observed in the PXRD data for the  $\text{KV}_6\text{Sb}_6$  phase; scanning electron microscopy data on the  $\text{KV}_6\text{Sb}_6$  pellet obtained via SPS; *in situ* high-temperature PXRD and DSC data that establishes the thermal stability of the  $\text{KV}_6\text{Sb}_6$  phase; comparison of the experimental HR-PXRD data for the  $\text{KV}_6\text{Sb}_6$  phase with monoclinic ( $C2/m$ ) and rhombohedral ( $R3m$ )

- models and results of Rietveld refinement for the rhombohedral model to validate the crystal structure of  $KV_6Sb_6$ ; comparison of the coordination environments of K, V, and Sb in  $V_3Sb_2$ ,  $KV_6Sb_6$ , and  $KV_3Sb_5$ ; additional magnetic property data for  $KV_6Sb_6$ ; details on hydride synthesis of the  $KV_3Sb_5$  phase including PXRD data and magnetic properties for  $KV_3Sb_5$ ; and Curie-Weiss fit of  $KV_6Sb_6$  susceptibility curve.
- [75] S. M. Kauzlarich, *Chemistry, Structure, and Bonding of Zintl Phases and Ions* (VCH Publishers Inc., New York, NY, USA, 1996).
- [76] T. F. Fässler, *Zintl Phases: Principles and Recent Developments. Book Series: Structure and Bonding* (Springer, Berlin, 2011), p. 139.
- [77] H. Zhang, L. Fang, M. B. Tang, Z. Y. Man, H. H. Chen, X. X. Yang, M. Baitinger, Y. Grin, and J. T. Zhao, Thermoelectric properties of  $Yb_xEu_{1-x}Cd_2Sb_2$ , *J. Chem. Phys.* **133**, 194701 (2010).
- [78] K. Guo, Q. G. Cao, X. J. Feng, M. B. Tang, H. H. Chen, X. Guo, L. Chen, Y. Grin, and J. T. Zhao, Enhanced thermoelectric figure of merit of Zintl phase  $YbCd_{2-x}Mn_xSb_2$  by chemical substitution, *Eur. J. Inorg. Chem.* **2011**, 4043 (2011).
- [79] P. Ren, Y. Liu, J. He, T. Lv, J. Gao, and G. Xu, Recent advances in inorganic material thermoelectrics, *Inorg. Chem. Front.* **5**, 2380 (2018).
- [80] A. Bhardwaj, A. Rajput, A. K. Shukla, J. J. Pulikkotil, A. K. Srivastava, A. Dhar, G. Gupta, S. Auluck, D. K. Misra, and R. C. Budhani,  $Mg_3Sb_2$ -based Zintl compound: A non-toxic, inexpensive and abundant thermoelectric material for power generation, *RSC Adv.* **3**, 8504 (2013).
- [81] E. S. Toberer, A. F. May, B. C. Melot, E. Flage-Larsen, and G. J. Snyder, Electronic structure and transport in thermoelectric compounds  $AZn_2Sb_2$  ( $A = Sr, Ca, Yb, Eu$ ), *Dalton Trans.* **39**, 1046 (2010).
- [82] F. Gascoin, S. Ottensmann, D. Stark, S. M. Haïle, and G. J. Snyder, Zintl phases as thermoelectric materials: Tuned transport properties of the compounds  $Ca_xYb_{1-x}Zn_2Sb_2$ , *Adv. Funct. Mater.* **15**, 1860 (2005).
- [83] B. Owens-Baird, S. Heinrich, and K. Kovnir, Thermoelectric materials, in *Encyclopedia of Inorganic and Bioinorganic Chemistry*, edited by R. A. Scott (Wiley, Hoboken, 2017).
- [84] J. A. Dolyniuk, B. Owens-Baird, J. Wang, J. V. Zaikina, and K. Kovnir, Clathrate thermoelectrics, *Mater. Sci. Eng. R* **108**, 1 (2016).